

MOF-Based Single-Atom and Metal Cluster Catalysts by Room-Temperature Synthesis for Tumor Therapy

Subin Yu, Haeun Kang, Seohyeon Jee, WooYeon Moon, Dohyub Jang, Wen-Tse Huang, Dongjun Kim, Kyungwha Chung, Dong-Il Won, Jungwon Park,* Ru-Shi Liu,* Kyungmin Choi,* Sehoon Kim,* Luke P. Lee,* and Dong Ha Kim*

Metal-organic frameworks (MOFs) are widely used as substrates for creating single-atom catalysts due to their abundance of ligands, facilitating enzymelike activity for biomedical applications. However, the high-temperature calcination process for single-atom catalysts limits economical, efficient, and large-scale synthesis. Here, a simple room-temperature synthesis of MOF-based single-atom and metal cluster catalysts is presented for tumor therapy. Fe/MOF is obtained through a coordination reaction at room temperature, while Au/MOF is synthesized from Au³⁺/MOF by introducing a reducing agent. Au/MOF effectively generates hydrogen peroxide (H₂O₂) from glucose, outperforming Au³⁺/MOF, and Fe/MOF subsequently produced hydroxyl radicals (•OH) by decomposing the generated H₂O₂via accelerated peroxidase-like activity in an acidic environment. In vitro and in vivo studies confirm a significantly enhanced cancer eradication ability compared to the PBS-treated group by combining cascade enzymatic activity, destruction of oxidative homeostasis, and excessive mitochondrial-mediated lipid peroxidation. The novel synthesis process of MOF-based metal single-atom catalysts establishes a new paradigm for fabricating effective enzyme-like nanomaterials for multimodal tumor therapy.

1. Introduction

Nanomaterials with natural enzyme-like properties have been widely considered reactive oxygen species (ROS)-based nanomedicine for catalytic tumor treatment. Noble metal and transition metals, including iron (Fe), palladium (Pd), platinum (Pt), ceria (Ce), gold (Au), and silver (Ag), have shown biological enzyme-like features such as peroxidase, catalase, oxidase, and superoxide dismutase, which all are involved in cellular redox homeostasis. These biocompatible enzyme-like nanomaterials effectively generate numerous ROS or mimic the glucose oxidase (GOD) to initiate the starvation of cancer cells.[1-3] Iron, typically a ferrous ion, has been recognized as a peroxidase-like nanomaterial, decomposing the hydrogen peroxide (H₂O₂) to ROS, especially hydroxyl radical (•OH), for contaminant elimination under an acidic environment.[4] ROS eradicate tumors by

S. Yu, H. Kang, D.-I. Won, L. P. Lee, D. H. Kim Department of Chemistry and Nanoscience Ewha Womans University Seoul 03760, Republic of Korea

E-mail: lplee@bwh.harvard.edu; dhkim@ewha.ac.kr

S. Yu, K. Chung, L. P. Lee Harvard Institute of Medicine Harvard Medical School Harvard University Brigham and Women's Hospital Boston, MA 02115, USA S. Jee, W. Moon, K. Choi

Department of Chemical and Biological Engineering

Sookmyung Women's University Seoul 043 10, Republic of Korea E-mail: kmchoi@sookmyung.ac.kr

Department of Biomicrosystem Technology Korea University Seoul 02841, Republic of Korea

The ORCID identification number(s) for the author(s) of this article can be found under https://doi.org/10.1002/adhm.202501058

DOI: 10.1002/adhm.202501058

D. lang, S. Kim Chemical and Biological Integrative Research Center Korea Institute of Science and Technology

5, Hwarang-ro 14-gil, Seongbuk-gu, Seoul 02792, Republic of Korea E-mail: sehoonkim@kist.re.kr

W.-T. Huang, R.-S. Liu Department of Chemistry National Taiwan University Taipei 106, Taiwan E-mail: rsliu@ntu.edu.tw

D. Kim, J. Park

School of Chemical and Biological Engineering

College of Engineering Seoul National University Seoul 08826, Republic of Korea

E-mail: jungwonpark@snu.ac.kr K. Chung, L. P. Lee

Department of Biophysics Institute of Quantum Biophysics Sungkyunkwan University Suwon, South Korea

KU-KIST Graduate School of Converging Science and Technology Korea University

Seoul 02841, South Korea

ADVANCED
HEALTHCARE
MATERIALS

21922559, D. Dowloaded from https://advanced.onlinelibrary.wiely.com/doi/10.1002/adhm. 20201088 by Korea Institute of Science, Wiley Online Library on [0.1062025]. See the Terms and Conditions (https://onlinelibrary.wiely.com/terms-and-conditions) on Wiley Online Library for use of use; OA articles are governed by the applicable Creative Commons

destroying cellular organelles and membranes and regulating cell signaling. On the other hand, gold (Au) has also been considered as enzyme-like nanomaterials that exhibit GOD-mimic activity to oxidize glucose to gluconic acid and $\rm H_2O_2$. However, the lack of high-performance with desirable catalytic activity hinders the enzyme-like nanomaterials-mediated therapeutic application due to the inherent surface defect of present nanomaterials to produce sufficient \bullet OH for efficient killing of cancer cells. [8.9] Additionally, limited $\rm H_2O_2$ availability or relatively high pH levels adversely affect catalytic activities, leading to a lack of \bullet OH production. [10.]

Single-atom catalysts (SACs) have been recognized as effective electrocatalysts and heterogeneous catalysts.[11,12] The characteristic benefit of SACs arises from combining the homogenous catalysts with the isolated active site and highly stable and recyclable heterogeneous catalyst features. The SACs showcase significantly enhanced catalytic performance in electrocatalvsis and chemical synthesis with enlarged specificity and activity at an atomic level of the active site.[13] Utilizing a single atom as a catalytic center can be beneficial in maximizing atom utilization in the catalytic system with high selectivity and reactivity.[11] Numerous approaches have been developed to synthesize the SAC, including the wet chemical, [14] spatial confinement, [15] sacrificial template, [16] and atom-trapping via high-temperature treatment.^[17] In brief, the wet chemical method needs the distribution of metal precursors on support materials, followed by calcinating ligands under high temperatures to activate the metal single atom. Spatial confinement means anchoring the metal atom on porous materials such as MOF and zeolitic-imidazolate-framework (ZIF). The sacrificial template method utilizes porous templates to isolate metal precursors with pyrolysis treatment. The high-temperature mediated atom trapping method indicates that the metal atoms anchor at the defect sites of N-doped support by evaporating the

L. P. Lee Department of Bioengineering University of California, Berkeley Berkeley, CA 94720, USA

L. P. Lee

Department of Electrical Engineering and Computer Science University of California, Berkeley Berkeley, CA 94720, USA

D. H. Kim

Basic Sciences Research Institute (Priority Research Institute) Ewha Womans University

52, Ewhayeodae-gil, Seodaemun-gu, Seoul 03760, Republic of Korea D. H. Kim

Nanobio•Energy Materials Center (National Research Facilities and Equipment Center)

Ewha Womans University

52, Ewhayeodae-gil, Seodaemun-gu, Seoul 03760, Republic of Korea

D. H. Kim

College of Medicine

Ewha Womans University

25, Magokdong-ro 2-gil, Gangseo-gu, Seoul 07804, Republic of Korea

D. H. Kim

Gradutate Program in Innovative Biomaterials Convergence Ewha Womans University

52 Ewhayeodae-gil, Seodaemun-gu, Seoul 03760, Republic of Korea

metal precursor. It is noted that the above-mentioned synthetic approaches require high-temperature treatment with supporting materials during the fabrication. Insoluble and cheap supports for manufacturing SAC include carbon, ceria, Al₂O₂, and metal-organic framework (MOF).[18] Among these, MOF possesses abundant ligands (e.g., N, O, P, and S-ligands), facilitating the production of the highly stable SAC with an additional metal coordination center.[19] Transition metal coordinated with N ligand mimics the natural enzymes chemically, geometrically, and electronically with great activity and selectivity. N-doped carbon materials, including graphene, porous carbons, nanofibers, and fullerenes, are widely used to fabricate the transition metal-nitrogen coordinated SAC under high reaction temperatures. Utilization of certain MOFs, instead of N-doped carbon materials, would precisely manipulate the location of metal-nitrogen coordinated active centers by controlling types and ratios of organic ligands during the preparation of MOF. However, the unavoidable technological obstacle for the natural enzyme mimicking SACs toward scalable synthesis mainly focuses on a green synthesis with a cost-effective approach. Until now, most SACs are prepared through high-temperature (700 – 1000 °C) pyrolysis treatment. Nevertheless, the challenge arises in the large-scale production of SACs due to the high energy costs associated with this high-temperature process, thereby restricting their broader applications.[20]

In this work, we developed MOF-based single-atom and metal nanoclusters using a simple room-temperature synthetic approach for tumor therapy (Figure 1). Specifically, we established a cascade enzymatic reaction system that incorporates peroxidase (POD)-mimic single Fe atom catalysts alongside glucose oxidase (GOD)-mimic Au nanocluster (Au NC) catalysts. We utilized a unique support for metal-nitrogen coordination, specifically a zirconium-based MOF (UiO-67-BPY) and N-doped carbon materials, metal oxides, and silica. A single Fe atom was isolated in the ultrasmall MOF by a lone-pair electron from nitrogen (referred to as Fe/MOF), while Au NC was loaded into the pores of the MOF (referred to as Au/MOF) (Figure 1a). The entire synthesis was conducted at room temperature, distinguishing the current protocol from conventional approaches. The Au/MOF as-prepared acted as a GOD-mimic for oxidizing glucose to gluconic acid and hydrogen peroxide (H₂O₂). Generated single Fe atoms decomposed additional H₂O₂ to produce •OH through a POD-like reaction. Furthermore, Au/MOF was modified with a mitochondrial targeting moiety (triphenylphosphonium, TPP) to facilitate the internalization of Au/MOF into the mitochondria. The resulting TPP-modified Au/MOF exhibited the ability to deplete glutathione (GSH), disrupting the redox balance inside the mitochondria and promoting excessive lipid peroxidation. Overall, catalytic activities were enhanced due to the acidic environment, additional H₂O₂ produced by Au/MOF, and redox imbalance via GSH depletion, which generated a sufficient amount of •OH to kill cancer cells. To further incorporate chemotherapy, an anticancer drug (doxorubicin, DOX) was introduced into the Fe/MOF (denoted as Fe/DOX/MOF), facilitating drug delivery due to high porosity (Figure 1b). Our system overcomes the conventional limitations of nanocatalysts and may represent a multimodal nanomedicine approach for cancer treatment.

© 2025 Wiley-VCH GmbH

21922659, 0, Downloaded from https://advanced.onlinelibrary.wiley.com/doi/10.1002/adhm.202501058 by Korea Institute Of Science, Wiley Online Library on [01.062025]. See the Terms and Conditions (https://onlinelibrary.wiley.com/erms

and-conditions) on Wiley Online Library for rules of use; OA articles are governed by the applicable Creative Commons

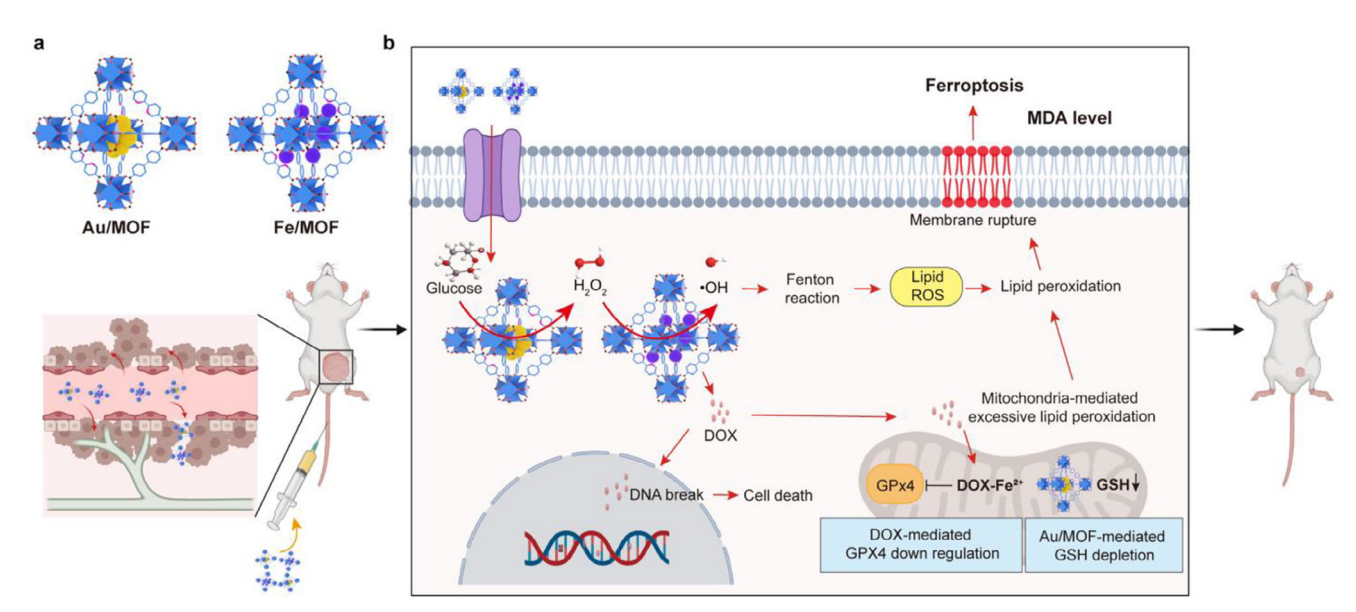


Figure 1. a) Schematic diagram of prepared Au/MOF and Fe/MOF. b) cascade enzymatic reaction mediated overall cell death mechanism. Fe/MOF induced the peroxidase-like activity, eventually leading to the ferroptosis of cancer cells. Simultaneously, delivered DOX caused the cell death via DNA break. In addition, DOX was accumulated in mitochondria for mitochondrial-mediated excessive lipid peroxidation. Besides, Au/MOF generated the H_2O_2 by decomposing the glucose to induce the starvation of cells. In addition, Au/MOF was uptaken by mitochondria to deplete GSH and cause additional oxidative stress to accelerate lipid peroxidation.

2. Results and Discussion

Zirconium-based metal-organic frameworks (UiO-67-BPY) were prepared using a solvothermal method by mixing ZrCl4 precursor, 4,4'-biphenyl-dicarboxylic acid (H2BPDC), and 2,2'bipyridine-5,5'dicarboxylate (H₂BPYDC) (Figure S1, Supporting Information).^[21] By introducing the bipyridine (BPY) docking centers, precisely controlled post-modifications are available to anchor the metal atoms and nanoclusters.[22] The single unit of prepared UiO-67-BPY and high-resolution transmission electron microscopy (HR-TEM) images with the Gaussian denoising process were depicted in Figure 2a,b. Based on HR-TEM, (002), (1), and (11) planes were observed from the Fourier transform (FFT) pattern along the [110] direction, well verifying the octahedra unit cell structure of UiO-67-BPY. The obtained denoised TEM presented the Zr node (bright) and ligands (dark) of UiO-67-BPY, well matched with the schematic of a single UiO-67-BPY unit. The obtained distance between the two of Zr node was around 0.12 nm, consistent with the length of BPY ligand (Figure 1b, left). Interestingly, an unexpected phenomenon in TEM was observed: the heavier elements appeared brighter, contrary to expectations based on atomic numbers. This phenomenon was investigated through TEM simulations varying both sample thickness and defocusing levels (Figure S2, Supporting Information). The results, as depicted, revealed an inversion phenomenon correlated with the degree of defocusing and sample thickness, contrary to the atomic numbers. This simulation provided evidence supporting the possibility of an inversion phenomenon observed in the experimental results. The scanning electron microscopy (SEM) image of prepared UiO-67-BPY showed a uniform polyhedral shape with an average size of 42 nm, suggesting the ultrasmall size MOF was well synthesized as the support of single atom and metal cluster (Figure S3a, Supporting Information).

Proton nuclear magnetic resonance (1H-NMR) result demonstrated the ratio between 4,4-biphenyl-dicarboxylic acid and 2,2'bipyridine-5,5'-dicarboxylate is 1:1, facilitating the isolation of a single atom in the solid supports (Figure S3b, Supporting Information). The crystallinity of prepared UiO-67-BPY was then assessed by X-ray diffraction (XRD) measurement and HR-TEM with FFT pattern (Figure S3c, Supporting Information). The characteristic peaks of 5.76°, 6.66°, and 9.46° were observed in the XRD pattern with sharp bands for (111), (200), and (220) planes, respectively, suggesting high crystallinity of UiO-67-BPY.[23,24] This result was well matched with the FFT pattern obtained from HR-TEM. To investigate the porosity of as-prepared UiO-67-BPY, we then measured the Brunauer-Emmett-Teller (BET) (Figure S3d, Supporting Information). UiO-67-BPY exhibited a BET surface area and total pore volume of 2257.3 m^2g^{-1} and 1.5687 cm³g⁻¹, respectively. The obtained average pore size was ≈2.75 nm. It indicated that UiO-67-BPY was an excellent carrier for drug and Au NC. Fourier transform infrared (FT-IR) measurement of UiO-67-BPY was conducted, and characteristic bands of carboxylate linker were monitored between 1300 and 1750 cm⁻¹, further supporting the successful formation of UiO-67-BPY MOF (Figure S3e, Supporting Information). In sum, nano-sized UiO-67-BPY were well prepared with precisely controlled ligand ratio and size as a unique support for producing single atom catalyst by formation of metal-nitrogen coordination bond.

We then prepared the GOD-like Au/MOF using UiO-67-BPY as a support material. We assume that introducing a single Au atom to UiO-67-BPY support would maximize the GOD-like activity. A single Au atom was incorporated into UiO-67-BPY support by mixing Au precursor and UiO-67-BPY solution via Au–N coordination (Au³⁺/MOF). Scanning transmission electron microscope (STEM) image and TEM image supported the successful formation of a single Au atom GOD catalyst (Figure 2d;

21922659, 0, Downloaded from https://advanced.onlinelibrary.wiley.com/doi/10.1002/adhm.202501058 by Korea Institute Of Science, Wiley Online Library on [01.062025]. See the Terms and Conditions (https://advanced.onlinelibrary.wiley.com/doi/10.1002/adhm.202501058 by Korea Institute Of Science, Wiley Online Library on [01.062025]. See the Terms and Conditions (https://advanced.onlinelibrary.wiley.com/doi/10.1002/adhm.202501058 by Korea Institute Of Science, Wiley Online Library on [01.062025]. See the Terms and Conditions (https://adhm.202501058).

and-conditions) on Wiley Online Library for rules of use; OA articles are governed by the applicable Creative Commons

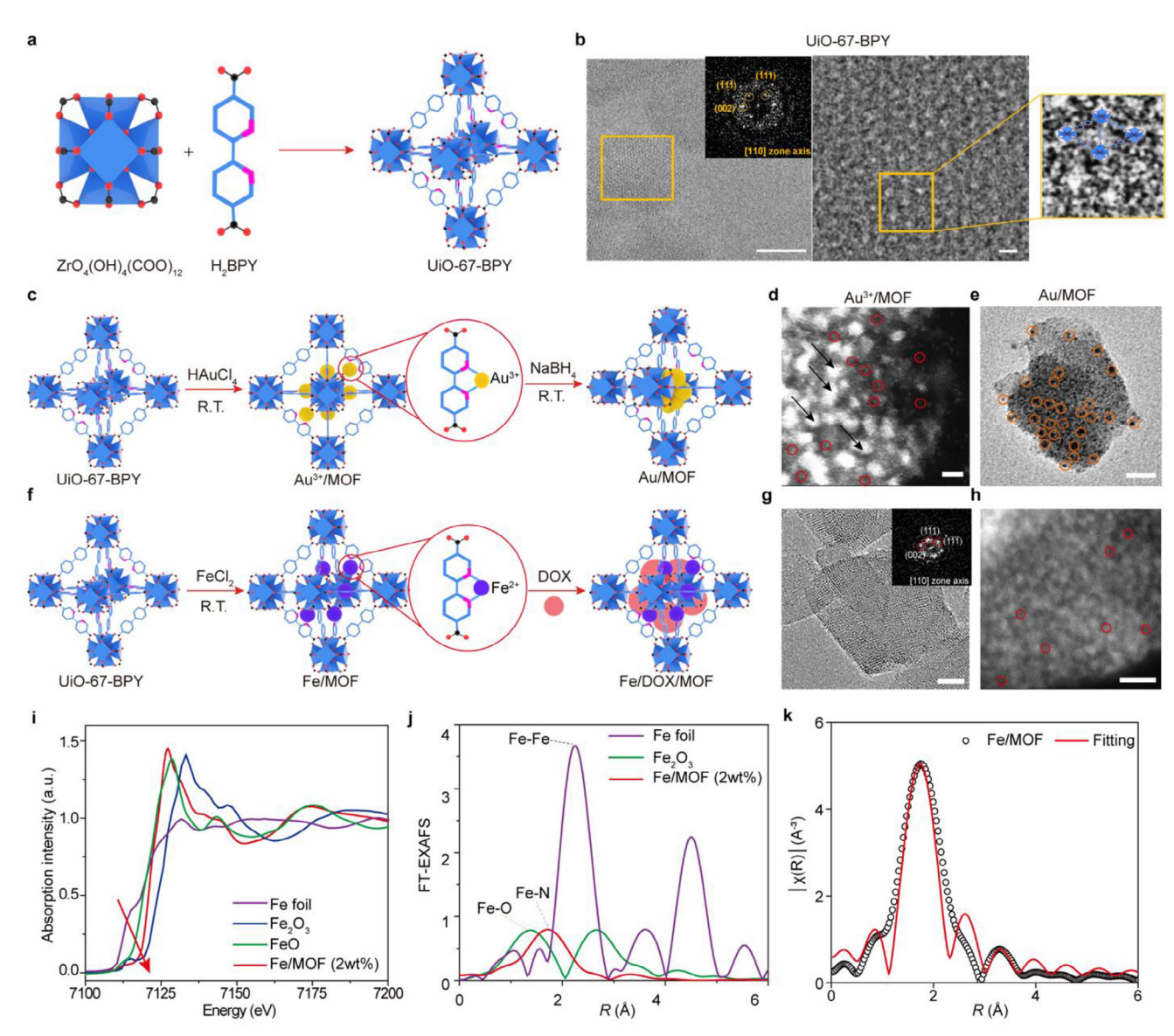


Figure 2. Characterization of Au/MOF and Fe/MOF. a) Schematic diagram of Zr-based metal–organic framework. b) HR-TEM of as-prepared UiO-67-BPY (scale bar = 20 nm). Inset: the FFT pattern of as-prepared UiO-67-BPY. Gaussian denoised TEM image of as-prepared UiO-67-BPY and mapping of their crystal structures (scale bar = 1 nm). c) Schematic diagram of Au/MOF preparation procedure. d) STEM image of Au 3 +/MOF (scale bar = 5 nm). The red circle indicates the single Au atom. The black arrow indicates the Zr metal site. e) TEM image of Au/MOF (scale bar = 10 nm). The orange circle indicates the gold nanocluster embedded in the MOF. f) Synthetic procedure of single Fe/DOX/MOF. g) TEM images of the as-prepared Fe/MOF (scale bar = 10 nm). Inset: the FFT pattern of as-prepared Fe/MOF. h) STEM images of the as-prepared Fe/MOF (scale bar = 5 nm). i) XANES spectra of Fe foil, Fe $_2$ O $_3$, FeO, and Fe/MOF (2 wt.%). j) FT-EXAFS spectra of Fe foil, Fe $_2$ O $_3$ and Fe/MOF (2 wt.%). k) Quantitative EXAFS fitting analysis of Fe/MOF (2 wt.%).

Figure S4a, Supporting Information). The GOD reaction was conducted, and the production of $\rm H_2O_2$ was confirmed by measuring the UV–vis absorbance of titanium oxysulfate (TiSO₄), an indicator for $\rm H_2O_2$. Colorless-TiSO₄ reacts with $\rm H_2O_2$ to form a yellow-colored peroxide-titanium complex, exhibiting UV–vis absorbance at 410 nm. After the GOD reaction with Au³+/MOF or Au NP, the spectra showed a characteristic peak at 410 nm, indicating the formation of $\rm H_2O_2$ by oxidizing glucose (Figure S4c, Supporting Information).

However, Au³⁺/MOF showcased a less efficient GOD-like activity than Au NP, contrary to our assumption. During the GOD

reaction, glucose lost its electrons through Au catalyst to form gluconic acid, and oxygen was used to earn two electrons from the catalyst to produce $\rm H_2O_2$. Our $\rm Au^{3+}/MOF$ facilitated the oxidization of glucose and the formation of Au metal rather than giving these electrons to surrounding oxygen (Figure S4b,d, Supporting Information). This finding demonstrated that the Au nanocluster is more favorable for the GOD-like performance than a single Au atom due to the GOD reaction requiring the multi-active site. [26] Thus, we decided to fabricate the Au NC in the UiO-67-BPY MOF instead of incorporating the single Au atom. Figure 2c describes the overall synthesis process of Au/MOF. The Au

www.advancedsciencenews.com

__ MATERIALS

www.advhealthmat.de

2025/25/9, Dowloaded from https://dvaluceed.onlinielibrary.wiley.com/doi/10.1002/adhm.2025/108. by Korea Institute of Science, Wiley Online Library on [01.05/2025]. See the Terms and Conditions (https://onlinelibrary.wiley.com/terms-and-conditions) on Wiley Online Library or rules of use; OA articles are governed by the applicable Creative Commons

precursors started nucleation to form Au NC at the lone-pair electron of the BPYDC ligand site due to high surface energy. Asprepared UiO-67-BPY MOF was re-dispersed in DMF solvent. and then the Au precursor and reducing agent were injected and stirred overnight. To incorporate the mitochondrial targeting ability, glycol chitosan-(3-carboxypropyl)triphenyl phosphonium bromide (GC-TPP) was then introduced via electrostatic interaction with polystyrene sulfonate (PSS) treated Au/MOF. TPP is a representative lipophilic cationic moiety that targets mitochondria, rapidly accumulating within mitochondria without a specific transportation mechanism.^[27] To confirm the structure of Au/MOF@GC-TPP, TEM and energy dispersive X-ray spectroscopy (EDX) were measured, as shown in Figure 2e and Figure S5 (Supporting Information). Au NC was homogeneously dispersed inside the MOF, and the average size was ≈8 nm. EDX mapping data showed that Zr and Au atoms were well distributed in the MOF, evidencing the successful preparation of Au/MOF. X-ray photoelectron spectroscopy (XPS) data of Au/MOF exhibited the binding energy for Au $4f_{7/2}$ and Au $4f_{5/2}$ at 84.0 and 87.71 eV, respectively, corresponding to the metallic Au, further confirming the formation of Au NC in the MOF (Figure S6a, Supporting Information). The optical property of Au/MOF was assessed as illustrated in Figure S6b (Supporting Information). Compared to the bare MOF (light orange line), after the incorporation of Au NC, a plasmonic band appeared at 540 nm, demonstrating the successful introduction of Au NC as GODmimic nanomaterials. FT-IR analysis of GC-TPP revealed the C-N stretching mode at 1232 cm⁻¹, proving the well-synthesized GC-TPP as a mitochondrial targeting moiety (Figure S6c, Supporting Information). To evaluate the surface modification of Au/MOF, zeta-potential was measured following the step-by-step ligand addition (Figure S6d, Supporting Information). Bare MOF displayed a slight negative charge, whereas a more pronounced negative zeta potential of PSS-modified MOF was detected. This result confirmed the introduction of PSS to MOF by Zr⁴⁺-SO₃⁻ interaction.[28] After introducing GC-TPP, MOF showcased the positive charge, demonstrating the well incorporation of GC-TPP onto the MOF surface by electrostatic interaction.

Next, we conducted the structural and optical characterization of POD-mimic Fe single atom MOF (Fe/MOF). The synthetic route was schematized in Figure 2f. As-prepared MOF was redispersed in a DMF solvent, and then Fe precursor was injected and kept undisturbed overnight at room temperature. HR-TEM and STEM images display the location of the Fe atom inside the MOF, as shown in red circles, demonstrating the anchoring of a single Fe atom inside the UiO-67-BPY MOF structures via metalbipyridine interaction (Figure 2g,h). EDX mapping data showed the atomic distribution profiles, further demonstrating the successful introduction of the Fe atom in the UiO-67-BPY MOF supports (Figure S7, Supporting Information). To further verify the single Fe atom, X-ray absorption near edge structure (XANES) and extended X-ray absorption fine structure (EXAFS) were measured (Figure 2i-k). We mixed the 2 and 5.5 wt.% of FeCl₂ with MOF solution. to optimize the Fe precursor amount. Compared to the 5.5 wt.% of FeCl₂, the oxidation state of the Fe atom in 2 wt.% was far higher, suggesting that 2 wt.% of Fe precursor was suitable for isolating the single Fe in the MOF supports (Figure S8a, Supporting Information; Figure 2i). Compared to the control groups (Fe foil, Fe₂O₃, and FeO), the energy position of our Fe/MOF (2 wt.%) was well-matched with FeO, indicating the oxidation states of Fe in our nanocatalyst corresponds to was +2 (Figure 2i). The atomic bond distance was investigated to confirm the atomic structure of Fe/MOF by EXAFS measurement (Figure 2j,k). In the case of 5.5 wt.% Fe precursor treated MOF, atomic distances of 2.6 Å were observed, corresponding to the Fe-Fe metal bond (Figure S8b, Supporting Information). Notably, MOF mixed with 2 wt.% of Fe precursor exhibited ≈1.72 Å bond distance correlated to the Fe-N bond, demonstrating the coordination of Fe with lone pair electrons from nitrogen, which are the ligands of constructing MOF (Figure 2k; Table S1, Supporting Information). Based on simulated EXAFS, estimated coordination structures of Fe-N, were obtained (Figure \$9 and Table S1, Supporting Information). The fitted average coordination number (CN) is 3.4; thus, the estimated coordination number between Fe and N could be either 3 or 4. We assume that the defect site of UiO-67-BPY existed due to the small size and branched BPY placed near intact BPY ligand to form Fe-N coordination bonding, inducing the slight distortion of overall structures, as illustrated in Figure \$9 (Supporting Information). These may result in the maintenance of Fe single-atom structures without the pyrolysis process. In sum, POD-mimic Fe/MOF was successfully produced by facile coordination chemistry at room temperature for mass production with UiO-67-BPY as support materials.

Considering the superior porosity of MOF, this property has facilitated the use of MOF as a drug carrier for target-specific chemotherapy. In this study, we loaded doxorubicin (DOX) as a representative chemotherapeutic drug inside the Fe/MOF cavity (denoted as Fe/DOX/MOF). UV-vis absorption was measured after loading DOX to the Fe/MOF to confirm the DOX loading (Figure \$10a,b, Supporting Information). We measured the concentration-dependent absorption spectra to investigate the DOX loading concentration and obtained the concentrationdependent standard curve. As shown in Figure \$10c (Supporting Information), compared to the Fe/MOF, a specific DOX absorption peak around 500 nm was detected in the presence of Fe/DOX/MOF, demonstrating the successful incorporation of DOX into the pores of Fe/MOF. Based on the standard curve for determining the loading concentration, the concentration of DOX loaded inside the MOF was around 0.1 mm. The timedependent DOX release profile was investigated under different pH conditions (Figure S10d, Supporting Information). Under acidic conditions, protonation weakens the electrostatic interactions between DOX and the MOF surface, thereby facilitating the faster release of DOX within 1 h, compared to the relatively moderate release observed under neutral pH conditions. These findings suggest that Fe/DOX/MOF facilitates the delivery of DOX to the tumor site, which can be site-specific due to the acidic microenvironment of a tumor.

Cascade enzymatic activities of Au/MOF and Fe/MOF combination were then examined (**Figure 3**). First, GOD-mimic properties of Au/MOF were evaluated by detecting generated $\rm H_2O_2$ using Amplex red assay (Figure 3a,d; Figure S11a, Supporting Information). Generated $\rm H_2O_2$ was reacted with Amplex red in the presence of horseradish peroxidase (HRP), and it converted into red fluorescent resorufin, exhibiting a fluorescence peak at 580 nm. ^[29] In the presence of Au/MOF with glucose, a significant resorufin fluorescence spectrum was monitored

21922659, 0, Downloaded from https://advanced.onlinelibrary.wiley.com/doi/10.1002/adhm.202501088 by Korea Institute Of Science, Wiley Online Library on [01.062025]. See the Terms and Conditions (https://onlinelibrary.wiley.com/terms

and-conditions) on Wiley Online Library for rules of use; OA articles are governed by the applicable Creative Commons

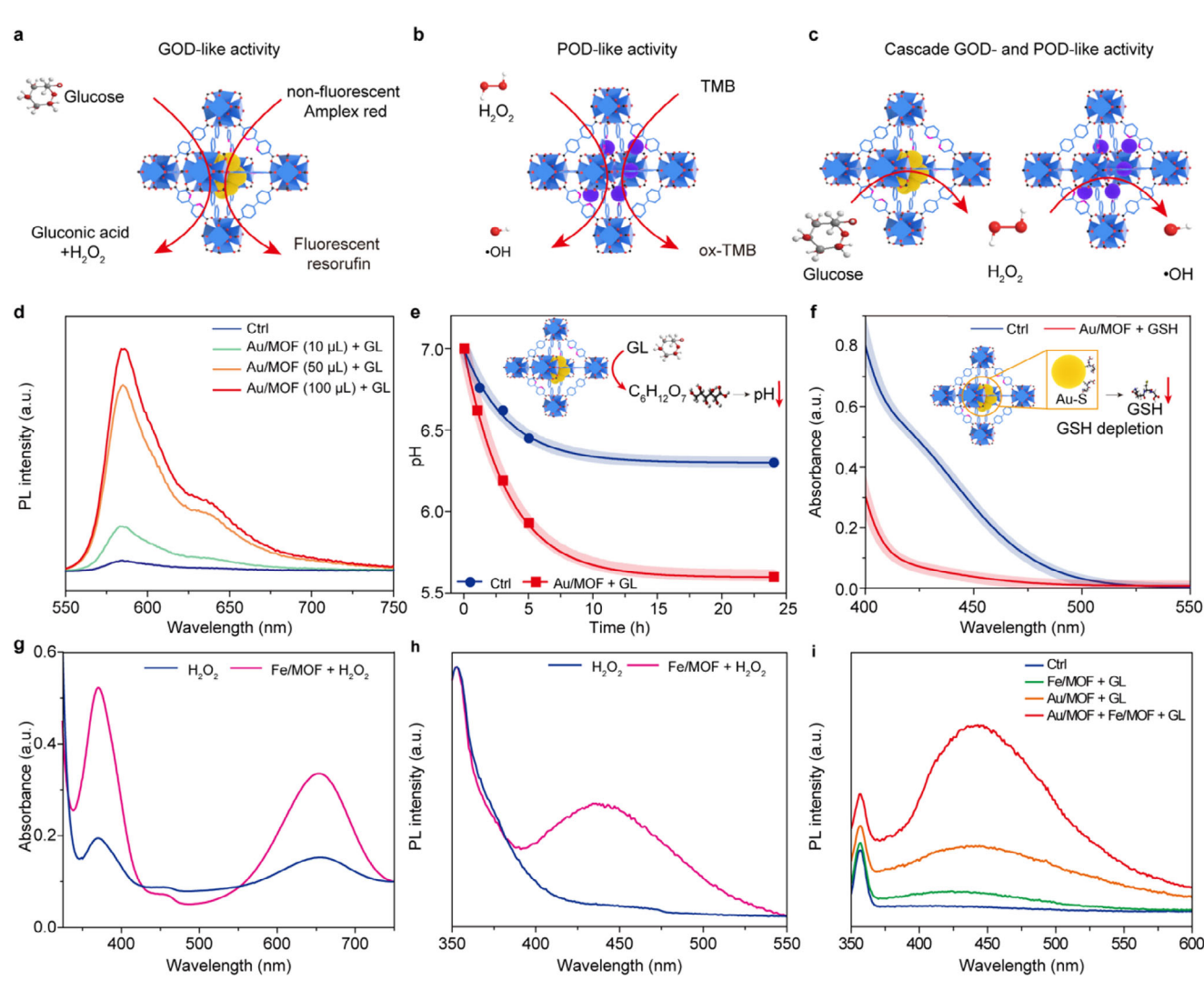


Figure 3. Enzymatic activities evaluation. a) Schematic illustration of Au/MOF mediated GOD-mimic reaction. Glucose was oxidized to form gluconic acid and H_2O_2 . Generated H_2O_2 was quantified by measuring the photoluminescence of resorufin. b) schematic illustration of Fe/MOF mediated POD-mimic reaction. H_2O_2 was decomposed to form hydroxyl radicals, and POD-mimic performance was examined by measuring the UV-vis absorption of TMB substrates. c) overall cascade enzymatic activity of Au/MOF and Fe/MOF. d) Glucose oxidase-like activity of Au/MOF with glucose. e) Time-dependent pH change profile of Au/MOF reacted with and without glucose f) Ellman's test for detection of GSH depletion ability of Au/MOF. g) Peroxidase-like activity of Fe-MOF with H_2O_2 . h) Photoluminescence spectra of Fe/MOF with H_2O_2 containing TA solution i) Photoluminescence spectra of TA solution containing various samples (Ctrl, Fe/MOF, Au/MOF, and Au/MOF + Fe/MOF) with glucose.

compared to the Au/MOF without glucose, demonstrating the generation of H_2O_2 via Au/MOF-mediated glucose oxidation. With increasing the Au/MOF amount, the overall fluorescence signal of resorufin also increased. To further examine the GOD-mimic properties of Au/MOF, we then monitored the gluconic acid production. Gluconic acid is another product of glucose oxidation, and the generation of gluconic acid was confirmed by monitoring the pH changes (Figure 3e). A fast pH decrease was detected in the presence of Au/MOF with glucose, verifying the generation of gluconic acid by oxidizing glucose via GOD-mimic Au/MOF. This resulted in the acidic environment of the tumor site, leading to the acceleration of the POD-like activity of Fe/MOF. Another valuable characteristic of Au/MOF is GSH depletion ability by forming Au—S bonding. [30] GSH is an essential antioxidant to preserve cell homeostasis and prevent

ROS-induced cell damage. GSH regulates mitochondrial lipid peroxidation by controlling glutathione peroxidase 4 (GPx4).^[31] Thus, depletion of GSH at the tumor site would be a valuable strategy to maximize oxidative stress and achieve excessive lipid peroxidation for stimulating ferroptosis. Au/MOF-mediated GSH depletion was interrogated via UV-vis absorption spectroscopy (Figure 3f). To determine the GSH depletion, Ellman's (5,5'-dithio-bis (2-nitrobenzoic acid), DTNB) assay was conducted. During the Ellman's assay, DNTB was reacted with GSH and produced yellow 5'-thio-2-nitrobenzoic acid (TNB) with maximal absorbance at 412 nm. ^[32] In the absence of Au/MOF, the solution containing GSH and DTNB showcased the absorption peak at 412 nm. In contrast, the GSH absorption peak disappeared in the presence of Au/MOF, confirming the GSH depletion ability of Au/MOF by forming Au-S

 $1.314 \times 10^{-9} \text{ M s}^{-1}$.

Online Library of conditions (https://onlinelbrary.wiley.com/doi/10.1002/adhm.202501088 by Korea Institute of Science, Wiley Online Library of (0.1060225]. See the Terms and Conditions (https://onlinelbrary.wiley.com/terms-and-conditions) on Wiley Online Library of rules of use; OA articles are governed by the applicable Creative Commons and Conditions (https://onlinelbrary.wiley.com/terms-and-conditions) on Wiley Online Library of rules of use; OA articles are governed by the applicable Creative Commons and Conditions (https://onlinelbrary.wiley.com/terms-and-conditions) on Wiley Online Library of rules of use; OA articles are governed by the applicable Creative Commons and Conditions (https://onlinelbrary.wiley.com/terms-and-conditions) on Wiley Online Library of rules of use; OA articles are governed by the applicable Creative Commons and Conditions (https://onlinelbrary.wiley.com/terms-and-conditions) on Wiley Online Library of rules of use; OA articles are governed by the applicable Creative Commons and Conditions (https://onlinelbrary.wiley.com/terms-and-conditions) on Wiley Online Library of rules of use; OA articles are governed by the applicable Creative Commons and Conditions (https://onlinelbrary.wiley.com/terms-and-conditions) on Wiley Online Library of rules of use; OA articles are governed by the applicable Creative Commons and Conditions (https://onlinelbrary.wiley.com/terms-and-conditions) on Wiley Online Library of the applicable Creative Commons and Conditions (https://onlinelbrary.wiley.com/terms-and-conditions) on Wiley Online Library of the applicable Creative Commons and Conditions (https://onlinelbrary.wiley.com/terms-and-conditions) on Wiley Online Library of the applicable Creative Commons and Conditions (https://onlinelbrary.wiley.com/terms-and-conditions) on Wiley Online Library of the applicable Creative Commons and Conditions (https://onlinelbrary.wiley.com/terms-and-conditions) on Wiley Online Library of the applicable Creative Commons and Conditions (https://onlinelbrary.wiley.com

interaction. Next, the POD-like activities of Fe/MOF were explored, as shown in Figure 3b,g,h. 3,3′,5,5′-tetramethylbenzidine (TMB) is a well-known substrate to detect POD-like activity by monitoring the absorption of oxidized-TMB (ox-TMB), which resulted from POD-like activity-induced H₂O₂ decomposition.^[33] Specific absorption peaks of ox-TMB at 370 and 650 nm were observed in the presence of Fe/MOF with H₂O₂ Meanwhile, the negligible peaks were detected in H₂O₂, affirming the POD-like activity of Fe/MOF (Figure 3g). To explore the reaction mechanism of Fe/MOF, time-dependent absorption changes of ox-TMB were monitored at varying H₂O₂ concentrations (0 – 800 mm). Based on these profiles, the Michaelis-Menten and Lineweaver-Burk kinetic models for Fe/MOF were derived (Figure \$12, Supporting Information). According to the Lineweaver-Burk equation (Equation 1)[34], the Michaelis-Menten constant (Km) for Fe/MOF was determined to be 89.8 mм while the maximum re-

$$\frac{1}{V} = \frac{Km}{Vmax} \frac{1}{|S|} + \frac{1}{Vmax} \tag{1}$$

action velocity (Vmax) for Fe/MOF with H2O2 was calculated as

Notably, the $V_{\rm max}$ of Fe/MOF exceeded that of HRP^[34] and previously reported Fe-N SACs,^[35] suggesting a more rapid and efficient decomposition of H_2O_2 at the single-atom active sites within the Fe/MOF framework. This superior catalytic performance highlights the effective stabilization and activation of single Fe atoms by the MOF structure, contributing to enhanced enzymatic mimicry compared to natural enzymes and other SAC systems.

To evaluate the •OH generation ability of Fe-MOF, the photoluminescence (PL) spectra of terephthalic acid (TA) in the presence of our samples were investigated (Figure 3h). TA is the •OH indicator, which reacted with •OH to generate the 2hydroxyterephthalic acid (TAOH) fluorescent molecules, exhibiting the PL spectrum at 450 nm.[36] The presence of Fe/MOF with H_2O_2 displayed a significant PL spectrum compared to the H_2O_2 only case, indicating the superior POD-like activities of Fe/MOF. Fe-MOFs exhibiting POD-like activity have also been shown to deplete intracellular GSH levels effectively.[37] We further assessed the additional GSH depletion efficiency of Fe/MOF, as shown in Figure \$13 (Supporting Information). The GSH absorption peak decreased in the presence of Fe/MOF compared to the control, suggesting that Fe/MOF possesses an additional GSH oxidizing ability of Fe/MOF through the production of •OH. Based on the individual enzymatic properties of Au/MOF and Fe/MOF, we assessed the cascade enzymatic activities of Au/MOF and Fe/MOF combination by monitoring the •OH generation using TA assay (Figure 3c). The presence of Au/MOF with glucose showcased the moderate PL peak at 425 nm, indicating the generation of H₂O₂ by decomposing the glucose via GODmimic Au/MOF (Figure 3i, orange line). In the presence of only Au/MOF, Fe/MOF, or Au/MOF + Fe/MOF without glucose, PL peaks of TAOH were not detected, implying no •OH was generated (Figure \$11b, Supporting Information). Notably, the presence of Au/MOF + Fe/MOF + glucose showcased the superior PL peak of TAOH compared to the other control groups, which demonstrated the cascade enzymatic activity of Au/MOF as a GOD-mimic and Fe/MOF as a POD-like activity to generate the •OH from glucose (Figure 3i, red line). Taken together, our hybrid catalytic system of both Au/MOF and Fe/MOF facilitated the induction of oxidative stress by decomposing glucose, which is the energy source of cells, to •OH for cancer treatment.

Having demonstrated the efficient cascade enzymatic activities of our nanomaterials, we investigated the potential of in vitro nanomedicine toward the CT26 cells by employing it in combinatorial catalytic therapeutics and chemotherapeutics for tumor treatment (Figure 4a). First, to verify the mitochondrial targeting ability of GC-TPP, we monitored the fluorescence images of MOF-GC-TPP-treated CT26 cells (Figure S14, Supporting Information). MitoTracker is a fluorogenic dye tracking the mitochondrial location, showing green fluorescence after staining the mitochondrial proteins. [38] Red fluorescent dye (Cvanine 5; Cy5) was loaded inside the MOF-GC-TPP and MOF-GC to observe the internalization properties of samples. After treating the as-prepared samples and MitoTracker dye to CT26 cells, we monitored the cell images using Nuance. Compared to the GCmodified MOF (MOF-GC) treated group, cells with MOF-GC-TPP exhibited colocalized green and red fluorescence signals. These results supported the superior mitochondrial targeting ability of TPP-modified GC, which would deliver the Au/MOF to mitochondria for the depletion of mitochondrial GSH to interfere the cellular redox balance. Based on the above results, we further examined the mitochondrial GSH depletion ability of Au/MOF-GC-TPP, as shown in Figure 4b. In the presence of Au/MOF-GC-TPP, the GSH level of mitochondria was significantly reduced compared to control groups, whereas negligible reduction was detected for all groups of cytosolic GSH level. These results support the possibility of mitochondrial excessive lipid peroxidation by down-regulation of GPx4 due to reduced GSH levels in mitochondria.[39] We assessed the cellular GODmimicking activity by measuring glucose levels to evaluate the effectiveness of Au/MOF at different concentrations (Figure S15, Supporting Information). CT26 cells treated with Au/MOF (0- $300~\mu g~mL^{-1}$) exhibited a substantial decrease in glucose levels, indicating the potent GOD-like activity of Au/MOF. The cell cytotoxicity of our enzyme-like nanomaterials was assessed by watersoluble tetrazolium salts (WST) assay with increasing concentration (final concentration of each sample: $0 - 125 \,\mu g \, mL^{-1}$). The WST solution was treated onto the CT26 cell after incubation of samples for 24 h, and the absorbance at 450 nm was then monitored to validate the cell viability. As shown in Figure 4c, only treated with Au/MOF -TPP or Fe/MOF-GC showed negligible cell cytotoxicity (red bar for Au/MOF-GC-TPP; light blue bar for Fe/MOF-GCs). Cells treated with Au/MOF-GC-TPP + Fe/MOF-GC exhibited decreased cell viabilities with increasing the sample concentration due to the generated •OH from tumor microenvironment abundant glucose via cascade enzymatic activities mediated by Au/MOF-GC-TPP and Fe/MOF-GC (Figure 4c, fuchsia bar). To confirm the therapeutic effect of DOX, cell cytotoxicity of Fe/DOX/MOF-GC was also monitored (Figure 4c, blue bar). With increasing the Fe/DOX/MOF-GC concentration, cell viabilities were decreased proportionally, indicating the chemotherapeutic effect of DOX, which was loaded inside the pore of MOF. Importantly, the presence of Au/MOF-GC-TPP + Fe/DOX/MOF-GC showcased the superior therapeutic effect compared to those of control groups, suggesting the combination of catalytic and chemotherapeutic effect of our enzyme-like nanomaterials via

21922559, Downloaded from https://advanced.onlinelibrary.wiey.com/doi/10.1002/adhm. 202501058 by Korea Institute Of Science, Wiley Online Library on [01.062025], See the Terms and Conditions (https://onlinelibrary.wiley.com/terms-and-conditions) on Wiley Online Library for rules of use; OA arches are governed by the applicable Creative Commons.

www.advhealthmat.de

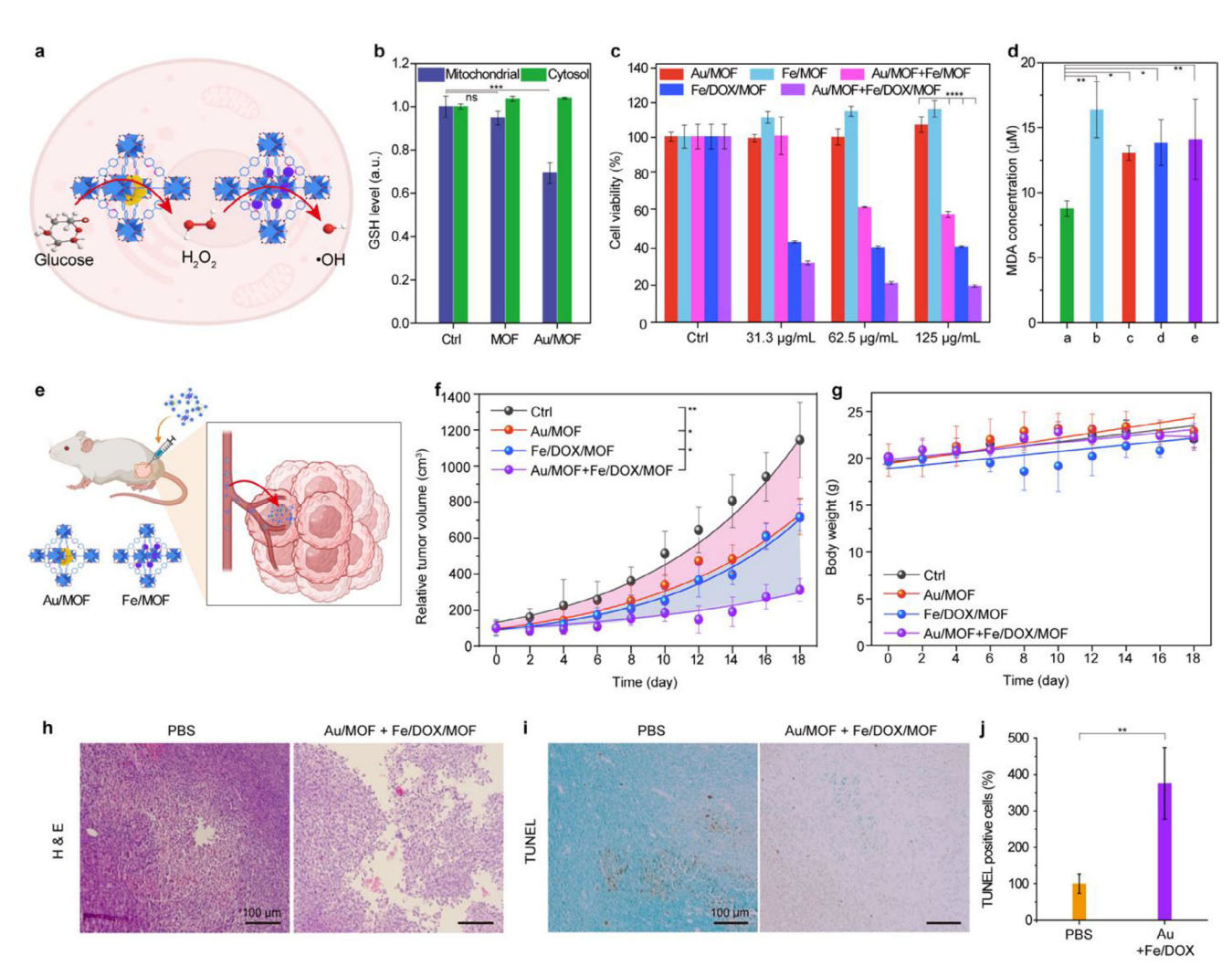


Figure 4. In vitro and in vivo study. a) Schematic diagram of in vitro experiment. b) Mitochondrial and cytosol GSH depletion ability test treated with bare MOF-TPP and Au/MOF-TPP. c) Cytotoxicity of various samples (Au/MOF, Fe/MOF, Fe/DOX/MOF, Au/MOF + Fe/MOF, and Au/MOF + Fe/DOX/MOF) treated CT26 cells in a concentration-dependent manner (final concentration of each sample: $0-125~\mu g~mL^{-1}$). d) MDA assay treated with a: Ctrl, b: Fe/MOF, c: Au/MOF, d: Fe/DOX/MOF and e: Au/MOF + Fe/DOX/MOF. e) Schematic illustration of in vivo experiments with bearing CT26 cells. f) Time-dependent tumor suppression profiles of tumor-bearing mice treated with PBS, Au/MOF, Fe/DOX/MOF, and Au/MOF + Fe/DOX/MOF (n=5). Tumor size was measured at an interval every 2 days. g) Body weight change profiles of mice treated with PBS, Au/MOF, Fe/DOX/MOF, and Au/MOF + Fe/DOX/MOF. Body weight was measured every 2 days interval. h) H&E staining of tumor treated with PBS and Au/MOF + Fe/DOX/MOF. i) TUNEL staining of tumor treated with PBS and s Au/MOF + Fe/DOX/MOF. j) Quantitative analysis of TUNEL-positive cells treated with PBS and Au/MOF + Fe/DOX/MOF. Statistical analysis was performed by one-way ANOVA test (****** p<0.0001, ***** p<0.001, **** p<0.001, *** p<0.001).

cascade enzymatic activities and efficient delivery of drugs for cancer treatment. The observed cytotoxicity results were further validated by live/dead cell imaging by using calcein-AM (green) and propidium iodide (PI, red), as shown in Figure S16 (Supporting Information). The green fluorescence from calcein-AM is observed only in the living cell with esterase. In contrast, the dead cell exhibits red fluorescence due to the permeable PI dye inside the cell nucleus.^[40] The control group revealed green fluorescence, whereas a red fluorescence signal was observed with our enzyme-like nanomaterials-treated groups. Importantly, cells treated with Au/MOF-GC-TPP + Fe/DOX/MOF-GC exhibited significant red fluorescence compared to other control groups, rectifying the above WST assay result. The cellular ROS levels were then investigated to confirm the ROS-generating

ability of our enzyme-like nanomaterials combinations (Figure S16, Supporting Information). Dichloro-dihydro-fluorescein diacetate (DCFH-DA) acts as a cellular ROS indicator, converting to DCFH by intracellular esterase and then transforming into fluorescent DCF (green) in the presence of ROS^[41] Fe/MOF-GC-only or Fe/MOF + Glu-treated cells exhibited no green fluorescence signals, suggesting that cellular ROS were not generated without glucose and Au/MOF. To mimic the TME, which naturally contains excess $\rm H_2O_2$, we added $\rm H_2O_2$ to confirm the combinational generation of \bullet OH through POD-like and cascade GOD-like reactions. Strong green signals were observed in cells treated with Fe/MOF + $\rm H_2O_2$, indicating that effective $\rm H_2O_2$ decomposition occurred via the POD-like activity of the prepared Fe/MOF. Compared to the PBS-treated group, cells incubated with



2025/25/9, Dowloaded from https://dvaluceed.onlinielibrary.wiley.com/doi/10.1002/adhm.2025/108. by Korea Institute of Science, Wiley Online Library on [01.05/2025]. See the Terms and Conditions (https://onlinelibrary.wiley.com/terms-and-conditions) on Wiley Online Library or rules of use; OA articles are governed by the applicable Creative Commons

Au/MOF-GC-TPP + Fe/MOF-GC + Glu also demonstrated strong green fluorescence. Interestingly, Au/MOF + Fe/MOF + Glu + $\rm H_2O_2$ exhibited the strongest ROS signal, indicating a combinational enhancement of ROS generation ability through the supply of additional $\rm H_2O_2$ by GOD-like Au/MOF. These results illustrate the generation of cellular ROS by decomposing glucose into \bullet OH via the cascade of enzymatic activities of our enzymelike nanomaterials.

To assess the cell death mechanism, we monitored the malondialdehyde (MDA) level of cells treated with our enzyme-like nanomaterials (Figure 4d). The MDA is the product of polyunsaturated lipid bilayer peroxidation.^[42] The level of MDA is usually used as an indicator of ferroptosis, and MDA production would be increased during the ferroptosis. As a result of Fe/MOF-GC being uptaken by cells, the MDA level was effectively increased compared to the control group, suggesting ferroptosis-mediated cell death. In the case of Au/MOF-GC-TPP, an increase in MDA level was observed compared to the PBS-treated group. These findings supported that the GSH depletion led to mitochondrialmediated lipid peroxidation. Recently, it is reported that DOXmediated cellular toxicity also relates to the down-regulation of GPx4, leading to mitochondrial ferroptosis. [43] Fe/DOX/MOF-GC treated group and Au/MOF-GC-TPP + Fe/DOX/MOF-GC treated one show the increased level of MDA molecules, verifying the effective cellular cytotoxicity mediated by our system via the combinatorial POD-mimic and mitochondria-mediated excessive lipid peroxidation, eventually leading to the ferroptosis. To investigate the downregulation of GPx4, we conducted immunofluorescent imaging of CT26 cells treated with various control groups (ctrl, Au/MOF + Fe/MOF, Fe/DOX/MOF, and Au/MOF + Fe/DOX/MOF) (Figure \$18, Supporting Information). The Au/MOF-GC-TPP + Fe/DOX/MOF-GC treated group showed a significantly reduced expression level of GPx4, further demonstrating mitochondrial ferroptosis. These results further support the cytotoxicity of our system described above. In conclusion, we deduce that the combination of Au/MOF-GC-TPP and Fe/DOX/MOF-GC has the potential to generate ROS, leading to a powerful anticancer effect without external stimulation, making it valuable for catalytic cancer therapy through excessive lipid peroxidation-mediated ferroptosis.

We then conducted in vivo study to validate the therapeutic efficacy of our enzyme-like nanomaterials, as depicted in Figure 4e. The time-dependent relative tumor volume is presented in Figure 4f. Treatment with only Au/MOF-GC-TPP or Fe/DOX/MOF-GC exhibited tumor suppression ability within 4 days of monitoring, but significant tumor recurrence was observed starting from day 6. This suggested that the sole use of Au/MOF-GC-TPP-mediated glucose consuming (starvation therapy) or the POD-mimic by Fe/DOX/MOF-GC in combination with chemotherapy was insufficient for complete tumor eradication. In stark contrast, the combination of Au/MOF-GC-TPP and Fe/DOX/MOF-GC demonstrated superior tumor suppression ability with minimal recurrence. These findings support that our system effectively facilitated tumor suppression by combining consumption of glucose-mediated starvation therapy, adequate H₂O₂ supplement with acidic conditions for PODmimic acceleration, chemotherapy, and depletion of mitochondrial GSH, leading to excessive oxidative stress and lipid peroxidation. Despite the significance of our system, the hypoxic conditions of the tumor microenvironment could limit the Au/MOFmediated GOD-like activities. Future studies need to demonstrate this by incorporating oxygen-generating components (e.g., MnO2 or catalase mimics) or oxygen carriers to solve current limitations.[44-47] No significant body weight changes were monitored during the treatment, indicating the biocompatibility of our system, as shown in Figure 4g. To further confirm the effective tumor suppression, hematoxylin and eosin (H&E) staining of tumor slices treated with Au/MOF-GC-TPP + Fe/DOX/MOF-GC and control groups was performed, as shown in Figure 4h. After 1 week of treatment, the mice were sacrificed, and tumor slices were obtained. The most significant tumor tissue damage was observed in the Au/MOF-GC-TPP + Fe/DOX/MOF-GC group compared to the PBS-treated group. This observation supported the synergistic tumor eradication ability of the cascade enzymatic reaction combined with starvation and the chemotherapeutic effect.

Furthermore, tumor tissue damage was evaluated using terminal deoxynucleotidyl transferase (TdT)-mediated deoxyuridine triphosphate (dUTP) nick end labeling (TUNEL) staining, and quantification analysis was performed (Figure 4i,i). The TUNEL positive signal was four times higher in the Au/MOF-GC-TPP + Fe/DOX/MOF-GC group compared to the PBStreated group, which aligns with the H&E staining results. Additional histological analysis was conducted to highlight the biosafety of our enzyme-like nanomaterials. The five major organs (lung, heart, liver, kidney, and spleen) were extracted from mice treated with PBS and Au/MOF-GC-TPP + Fe/DOX/MOF-GC. As shown in Figure S19 (Supporting Information), no severe tissue damage or organ morphological alterations were observed, indicating the biocompatibility of our enzyme-like nanomaterials. These findings strongly support that our enzymelike nanomaterials specifically target the tumor region without causing nonspecific tissue damage. In summary, the in vivo study further validated the remarkable therapeutic potential of our system in generating ROS with excessive oxidative stress for combinatorial catalytic, chemo-, and starvation cancer therapy.

3. Conclusion

In this contribution, we presented ultrasmall UiO-67-BPY MOFbased SAC produced through a simple mixing method at room temperature. A single Fe atom was anchored to the lone-pair electrons of nitrogen in the MOF to form stable Fe-N bonding, while Au NC was introduced instead of a single Au atom due to the necessity of a multi-active site during the GOD reaction. The combination of Au/MOF and Fe/MOF induced a cascade of enzymatic reactions in living systems. To take advantage of the abundant porosity of MOFs, we loaded a cancer drug, doxorubicin (DOX), into the Fe/MOF, creating Fe/DOX/MOF. To disrupt the homeostasis of the cellular redox system, Au/MOF was further modified with a mitochondrial targeting moiety to deplete GSH. These changes resulted in an imbalance of the redox system and excessive mitochondrial lipid peroxidation. The constructed Fe/MOF exhibits an oxidation state of 2+ with Fe-N_{3.4} coordination bonds, demonstrating well-established POD properties. The overall cascade of enzymatic activity effectively generates •OH from glucose as the substrate. Gluconic acid further induces an acidic

ADVANCED
HEALTHCARE
MATERIALS

21922659, 0, Downloaded from https://advanced.onlinelibrary.wiley.com/doi/10.1002/admm.202501058 by Korea Institute Of Science, Wiley Online Library on [01.062025]. See the Terms and Conditions (https://onlinelibrary.wiley.com/errns

-and-conditions) on Wiley Online Library for rules of use; OA articles are governed by the applicable Creative Commons

environment, accelerating the POD-mimic reaction. In vitro studies confirmed the practical therapeutic effect of the cascade glucose oxidation and •OH generation in eradicating cancer cells. Depleting GSH and Fe²⁺-induced lipid peroxidation ultimately leads to ferroptosis. In vivo studies further validate our system's four-fold enhanced therapeutic efficacy compared to the PBS-treated group. Our novel and straightforward synthesis process of UiO-67-BPY MOF-based SAC and metal clusters represents a new paradigm for fabricating single-atom enzyme-like nanomaterials for multimodal cancer treatment.

4. Experimental Section

Chemicals: Gold(III) chloride trihydrate (HAuCl₄•3H₂O; ≥99.9% trace metals basis), iron (II) chloride tetrahydrate (FeCl₂•4H₂O, ≥99.99% trace metals basis), sodium borohydride (NaBH₄, ≥99.99% trace metals basis), sodium hydroxide (NaOH, 98%), N,N-Dimethylformamide (anhydrous, 99.8%), ethanol (C₂H₆O, 99%), 3,3′,5,5′-Tetramethylbenzidine (TMB, ≥99%), terephthalic acid (TA, 98%), 2′,7′- Dichlorodihydrofluorescein diacetate (DCFH-DA, ≥97%), phosphate buffered saline tablet (PBS), sodium acetate (>99%), hydrochloric acid (HCl, ACS reagent, 37%), glacial acetic acid (pharmaceutical secondary standard), peroxide assay kit, Live/Dead cell double staining, and Lipid peroxidation (MDA) assay kit were all purchased from Sigma—Aldrich. Hydrogen peroxide (H₂O₂, 30%) was purchased from Junsei Chemical Co. Ltd. MTT assay kit (EZ-cyTox) from Daeil Lab Service Co. Ltd, Republic of Korea. The solvents were used as received and without any further purification.

Instruments and Measurements: Transmission electron microscopy (TEM) images were collected from a JEOL JSM2100-F microscope operated at 100 K. Elemental analysis and mapping were accomplished by energy dispersive X-ray spectroscopy (EDX) using a JEOL JEM-3011 at an accelerating voltage of 200 kV. Scanning electron microscopy (SEM) images were taken using JEOL JSM6700-F. UV—vis absorbance spectra measurements were conducted on a Varian Cary5000 UV—vis—NIR spectrophotometer. Cell viability tests were done using an Infinite M200 PRO microplate reader. Photoluminescence (PL) spectra were collected using a PerkinElmer LS 55 spectrofluorimeter at room temperature. X-ray absorption spectroscopy (XAS) was collected from the TPS 44A and TLS 17C1 beamlines of the National Synchrotron Radiation Research Center (NSRC) in Hsinchu, Taiwan. The storage works at 1.5 GeV with a beam current of 360 mA at TLS. Fluorescence mode was used to collect the XAS spectra in the Fe K-edge.

Multi-Slice TEM Simulation: Simulated TEM images for UiO-67, with a consistent size of 2.7 nm and varying thickness, were generated using multi-slice TEM simulation, as detailed in references 1 and 2. Simulated TEM images were obtained from a tetragonal supercell measuring 26.56 Å \times 26.56 Å \times 5–13 Å, with a pixel size of 0.166 Å. The super cells were split into multiple 1.0-Å-thick slices along the z-axis, with 256 \times 256 pixels sampling in the x and y axes. Key simulation parameters included an acceleration voltage of 200 kV, condenser aperture of 20 mrad, objective aperture of 100 mrad, C3 aberration of 1 μ m, incoherence effects of 3 nm, and spatial incoherence of 0.3 mrad. The resulting simulated TEM images were displayed with maximum contrast, mapping image intensities to the full grayscale range of 0 to 255. This comprehensive simulation approach allows for a detailed investigation of UiO-67 structural and morphological features, providing valuable insights for comparison with experimental TEM images.

Preparation of Zirconium-Based Metal-Organic Framework (MOF): First, ZrCl₄ (9.3 mg, 0.04 mmol) was dissolved in N,N'-dimethylformamide (DMF, 5 mL) with acetic acid (0.5 mL) in a 20 mL glass vial. The ligand solution was prepared by combining biphenyl-4,4'-dicarboxylic acid, 2,2'-bipyridine-5,5'-dicarboxylic acid, and DMF (5 mL). The well-dispersed ligand solution was then added to the metal solution, and the sealed vial was placed in an 85 °C oven for 12 h without exposure to light. Afterward, it was cooled to room temperature, and the solid was separated using a centrifuge (8000 rpm for 10 min). The product was

washed once with DMF and three times with methanol. Following the washing steps, the product was dried in a vacuum oven.

Preparation of a Single-Atom Coordinated MOF: The synthesized MOF (1 mg mL $^{-1}$) was dispersed in DMF and mixed with FeCl $_2$ (1 mg mL $^{-1}$). The ratio of MOF to FeCl $_2$ was adjusted to achieve a concentration of 2 wt.%. After incubating for one day, the mixture was washed using centrifugation.

Preparation of Gold Cluster-Embedded MOF: The synthesized MOF (1 mg mL $^{-1}$) was dispersed in DMF and mixed with HAuCl $_4$ (1 mg mL $^{-1}$). The mixture was incubated for one day. After incubation, residual HAuCl $_4$ was removed using centrifugation. Then, NaBH $_4$ (0.6 M) was added, and the mixture was stirred overnight. Washing was performed using centrifugation.

Cascade Enzymatic Activity Test: The Fenton-like ability of Fe/MOF nanostructures was monitored by colorimetric assay using 3,3',5,5'-tetramethylbenzidine (TMB). The Fe/MOF was suspended in a $0.1\,\mathrm{M}$ acetate buffer (pH 4.5), and TMB and $\mathrm{H_2O_2}$ were added to obtain a final concentration of 80 mM for each. The reaction was conducted at a constant temperature (35 °C). The UV–vis absorption was monitored.

The glucose-mimicking Au/MOF activity was monitored by measuring the fluorescence of Amplex Red with and without glucose. Au/MOF (1 mg mL $^{-1}$), D-glucose (0.1 M), and Amplex Red solutions were mixed and incubated for 30 min at 35 °C. Amplex Red was converted to fluorescence resorufin in the presence of H_2O_2 and horseradish Peroxidase. The cascade enzymatic activities of both single Fe/MOF and Au/MOF were then monitored by measuring the fluorescence of terephthalic acid (TA). Au/MOF, Fe/MOF, D-glucose (0.1 M), and TA solutions were mixed well and incubated for 30 min at 35 °C. After the reaction, fluorescence at 450 nm was measured under 315 nm excitation.

In Vitro Cell Test: Colon cancer cells (CT26) were obtained from the Korean Cell Line Bank and cultured in Roswell Park Memorial Institute Medium (RPMI 1640) supplemented with 10% fetal bovine serum and 1% antibiotic-antimycotic solution. The cells were maintained at 37 $^{\circ}\text{C}$ in a 5% CO $_2$ atmosphere.

Assay of Cellular and Mitochondrial GSH Levels: CT26 cells were treated with various formulations, harvested, and lysed. The lysates were centrifuged at 11 000 r.p.m. for 10 min, and the resulting supernatant was utilized for GSH detection. To quantify the GSH concentration, 0.2 mL of the supernatant was combined with 1 mL of 0.5 mm DTNB, and the absorbance was measured at 405 nm. The GSH levels in cells treated with nanoparticles were compared to the baseline GSH levels in untreated CT26 cells. For mitochondrial GSH measurements, mitochondria were isolated and lysed using a mitochondria isolation kit. The GSH levels in the lysates were assessed following the same protocol used for cellular GSH determination. Mitochondria extraction was performed according to the manufacturer's instructions.

Glucose Concentration Analysis: CT26 cells were plated in 96-well plates at a density of 1×10^4 cells per well and cultured for 24 h. Subsequently, the cells were treated with Au/MOF (0 – 300 $\mu g\ mL^{-1}$) and incubated for 24 h. According to the manufacturer's protocol, glucose levels were then measured using a glucose assay kit (Abcam, ab65333).

In Vivo Tumor Suppression Test: Balb/c nude mice were allowed to stabilize for 1 week prior to CT26 inoculation. Balb/c nude mice were subcutaneously injected with 1×10^6 CT26 cells. Once the tumor size reached 100 mm³, the therapeutics (the final concentration of each sample was 125 µg mL $^{-1}$) were peritumorally injected into the tumor region. For the initial 4 days, the therapeutics were injected every 2 days to optimize the therapeutic effectiveness. Tumor size was monitored at 2-day intervals for 18 days, and the mice were sacrificed for further analysis. All animal experiments were conducted in compliance with relevant laws and institutional guidelines of the Korea Institute of Science and Technology (KIST) and were approved by institutional committees (approval number: KIST-2020-073).

TUNEL Assay: To confirm apoptosis in the sample-treated tumor tissue, a TUNEL assay was conducted. The analysis utilized a commercially available TUNEL kit (ab206386, Abcam, Cambridge, USA). All procedures were carried out following the manufacturer's instructions. Photomicrographs were taken using an optical microscope.

21922659, 0, Downloaded from https://advanced.onlinelibrary.wiley.com/doi/10.1002/adhm.202501058 by Korea Institute Of Science, Wiley Online Library on [01.062025]. See the Terms and Conditions (https://onlinelibrary.wiley

and-conditions) on Wiley Online Library for rules of use; OA articles are governed by the applicable Creative

Supporting Information

Supporting Information is available from the Wiley Online Library or from the author.

Acknowledgements

This work was supported by the National Research Foundation (NRF) of Korea Grant funded by the Korean Government (2022R 1C 1C 2005931, 2021R 1C 1C 2003417), by the Basic Science Research Program (Priority Research Institute) funded by the Ministry of Education (2021R 1A 6A 1A10039823), and by the Korea Basic Science Institute (National Research Facilities and Equipment Center) grant funded by the Ministry of Education (2020R 1A 6C 101B194).

Conflict of Interest

The authors declare no conflict of interest.

Author Contributions

S.Y. and H.K. contributed equally to this work. D.H.K conceived the concept and supervised the project. L.P.L. supervised the project. S.K. provided the experimental facilities and supervised the project. S.Y. developed the concrete strategies, conducted the main experiments, analyzed the data, and wrote the manuscript. H.K. conducted the synthesis of the components and in vivo experiments. D.J. assisted the in vivo experiment. S.J., W.M., and K.C. provided the materials and conducted the characterization. W.-T.H. and R.-S.L. conducted the structural characterization. D.K. and J.P. conducted the main morphological characterization. K.C., D.-I.W., assisted the part of the diverse property tests. All the authors contributed to the preparation of the manuscript.

Data Availability Statement

The data that support the findings of this study are available from the corresponding author upon reasonable request.

Keywords

glucose oxidase mimic, metal-organic framework, peroxidase mimic, single atom catalyst, tumor therapy

> Received: February 26, 2025 Revised: April 28, 2025 Published online:

- [1] Y. Dai, Y. Ding, L. Li, Chin. Chem. Lett. 2021, 32, 2715.
- [2] M. Wang, M. Chang, C. Li, Q. Chen, Z. Hou, B. Xing, J. Lin, Adv. Mater. 2022, 34, 2106010.
- [3] W. Zhen, Y. Liu, W. Wang, M. Zhang, W. Hu, X. Jia, C. Wang, X. Jiang, Angew. Chem., Int. Ed. 2020, 59, 9491.
- [4] L. Gao, J. Zhuang, L. Nie, J. Zhang, Y. Zhang, N. Gu, T. Wang, J. Feng, D. Yang, S. Perrett, Nat. Nanotech. 2007, 2, 577.
- [5] Z. Zhou, J. Song, L. Nie, X. Chen, Chem. Soc. Rev. 2016, 45, 6597.
- [6] X. Zeng, Y. Ruan, Q. Chen, S. Yan, W. Huang, Chem. Eng. J. 2023, 452,
- [7] M. C. Ortega-Liebana, J. Bonet-Aleta, J. L. Hueso, J. Santamaria, Catalysts 2020, 10, 333.

- [8] M. Huo, L. Wang, Y. Wang, Y. Chen, J. Shi, ACS Nano 2019, 13, 2643.
- [9] S. Gao, H. Lin, H. Zhang, H. Yao, Y. Chen, J. Shi, Adv. Sci. 2019, 6, 1801733.
- [10] H. Zhou, X. Li, D. Niu, Y. Li, X. Liu, C. Li, W. Si, J. Cao, Y. Song, G. Wen, Adv. Healthcare Mater. 2021, 10, 2002126.
- [11] H. Zhang, G. Liu, L. Shi, J. Ye, Adv. Energy Mater. 2018, 8,
- [12] M. B. Gawande, K. Ariga, Y. Yamauchi, Small 2021, 17, 2101584.
- [13] L. Peng, L. Shang, T. Zhang, G. I. N. Waterhouse, Adv. Energy Mater. 2020, 10, 2003018.
- [14] L. Lin, W. Zhou, R. Gao, S. Yao, X. Zhang, W. Xu, S. Zheng, Z. Jiang, Q. Yu, Y.-W. Li, C. Shi, X.-D. Wen, D. Ma, Nature 2017, 544, 80.
- [15] Y. Liu, X. Wu, Z. Li, J. Zhang, S.-X. Liu, S. Liu, L. Gu, L. R. Zheng, J. Li, D. Wang, Y. Li, Nat. Commun. 2021, 12, 4205.
- [16] H. Shin, J. Ko, C. Park, D. H. Kim, J. Ahn, J. S. Jang, Y. H. Kim, S. H. Cho, H. Baik, I. D. Kim, Adv. Funct. Mater. 2022, 32, 2110485.
- [17] Z. Huang, T. Ban, Y. Zhang, L. Wang, S. Guo, C.-R. Chang, G. Jing, Appl. Catal., B 2021, 283, 119625.
- [18] Z. Li, D. Wang, Y. Wu, Y. Li, Natl. Sci. Rev. 2018, 5, 673.
- [19] P. Xia, C. Wang, Q. He, Z. Ye, I. Sirés, Chem. Eng. J. 2023, 452, 139446.
- [20] B. Chang, L. Zhang, S. Wu, Z. Sun, Z. Cheng, Chem. Soc. Rev. 2022, 51, 3688.
- [21] U. J. Ryu, S. J. Kim, H.-K. Lim, H. Kim, K. M. Choi, J. K. Kang, Sci. Rep. **2017** 7 612
- [22] T. N. Tu, M. V. Nguyen, H. L. Nguyen, B. Yuliarto, K. E. Cordova, S. Demir, Coord. Chem. Rev. 2018, 364, 33.
- [23] Z. Xu, G. Zhao, L. Ullah, M. Wang, A. Wang, Y. Zhang, S. Zhang, RSC Adv. 2018, 8, 10009.
- [24] D. Chen, J. Bi, J. Wu, A. Kumar, J. Inorg. Organomet. Polym. Mater. 2020, 30, 573.
- [25] A. Fatoni, D. W. Dwiasi, M. D. Anggraeni, J. Phys.: Conf. Ser. 2020, 1494, 012026.
- [26] J. Chen, Q. Ma, M. Li, D. Chao, L. Huang, W. Wu, Y. Fang, S. Dong, Nat. Commun. 2021, 12, 3375.
- [27] S. S. Liew, X. Qin, J. Zhou, L. Li, W. Huang, S. Q. Yao, Angew. Chem., Int. Ed. 2021, 60, 2232.
- [28] J. Zhong, R. K. Kankala, S.-B. Wang, A.-Z. Chen, Polymers 2019, 11,
- [29] V. Mishin, J. P. Gray, D. E. Heck, D. L. Laskin, J. D. Laskin, Free Radical Biol. Med. 2010, 48, 1485.
- [30] N. Gong, X. Ma, X. Ye, Q. Zhou, X. Chen, X. Tan, S. Yao, S. Huo, T. Zhang, S. Chen, Nat. Nanotech. 2019, 14, 379.
- [31] F. Ursini, M. Maiorino, Free Radical Biol. Med. 2020, 152, 175.
- [32] I. Rahman, A. Kode, S. K. Biswas, Nat. Protoc. 2006, 1, 3159.
- [33] X. Cao, H. Yang, Q. Wei, Y. Yang, M. Liu, Q. Liu, X. Zhang, Inorg. Chem. Commun. 2021, 123, 108331.
- [34] W. Yin, J. Yu, F. Lv, L. Yan, L. R. Zheng, Z. Gu, Y. Zhao, ACS Nano 2016, 10. 11000.
- [35] B. Xu, S. Li, L. Zheng, Y. Liu, A. Han, J. Zhang, Z. Huang, H. Xie, K. Fan, L. Gao, Adv. Mater. 2022, 34, 2107088.
- [36] Y. Zhang, N. Zhang, T. Wang, H. Huang, Y. Chen, Z. Li, Z. Zou, Appl. Catal., B 2019, 245, 410.
- [37] X. Gao, H. Wei, W. Ma, W. Wu, W. Ji, J. Mao, P. Yu, L. Mao, Nat. Commun. 2024, 15, 7915.
- [38] M. Poot, Y.-Z. Zhang, J. A. Krämer, K. S. Wells, L. J. Jones, D. K. Hanzel, A. G. Lugade, V. L. Singer, R. P. Haugland, J. Histochem. Cytochem. **1996**, 44, 1363.
- [39] M. Chu, X. An, C. Fu, H. Yu, D. Zhang, Q. Li, X. Man, X. Dai, Z. Li, Frontiers in Bioscience-Landmark 2023, 28, 186.
- [40] R. Gatti, S. Belletti, G. Orlandini, O. Bussolati, V. Dall'Asta, G. C. Gazzola, J. Histochem. Cytochem. 1998, 46, 895.
- [41] A. Aranda, L. Sequedo, L. Tolosa, G. Quintas, E. Burello, J. V. Castell, L. Gombau, Toxicol. In Vitro 2013, 27, 954.



ADVANCED
HEALTHCARE
MATERIALS

21922659, 0, Downloaded from https://advanced.onlinelibrary.wiley.com/doi/10.1002/adhm.202501088 by Korea Institute Of Science, Wiley Online Library on [01.06.2025]. See the Terms

and-conditions) on Wiley Online Library for rules of use; OA articles are governed by the applicable Creative Commons

www.advancedsciencenews.com

www.advhealthmat.de

- [42] P. Lei, T. Bai, Y. Sun, Front. physiol. 2019, 10, 139.
- [43] T. Tadokoro, M. Ikeda, T. Ide, H. Deguchi, S. Ikeda, K. Okabe, A. Ishikita, S. Matsushima, T. Koumura, K.-i. Yamada, JCI insight 2020, 5, e132747.
- [44] Y. Cheng, Y. D. Xia, Y. Q. Sun, Y. Wang, X. B. Yin, Adv. Mater. 2024, 36, 2308033.
- [45] M. Bai, T. Wang, Z. Xing, H. Huang, X. Wu, M. Adeli, M. Wang, X. Han, L. Ye, C. Cheng, *Nat. Commun.* 2024, 15, 9592.
- [46] M. Jin, Z. Liang, Y. Huang, M. Zhang, H. Fu, B. Wang, J. Guo, Q. Yang, H. Fang, J.-C. Liu, J. Am. Chem. Soc. 2024, 146, 34092.
- [47] X. Wang, Q. Li, Z. Zhao, L. Yu, S. Wang, H. Pu, M. Adeli, L. Qiu, P. Gu, L. Li, Adv. Funct. Mater. 2024, 34, 2313143.